

Check for updates

Interior Morphology and Pore Structure in High Surface Area Carbon Catalyst Supports

Robin Girod* and Vasiliki Tileli*

In proton exchange membrane fuel cells, the interior porosity of the standard high surface area carbon (HSC) supports anchors and shields catalysts, offering benefits in performance and durability. Yet, these carbons also add mass transport resistance. This delicate tradeoff relies on their interior diffusion pathways, which are difficult to fully characterize and remain poorly understood. Here, the multiscale morphology of HSCs is reported using full-range electron tomography, resolving features down to single carbon planes. It is found that the supports typically feature a core-shell morphology with large central pores and compact shell in which pores are slit-shaped and sub-nm in size, while entry points are 7–8 Å in diameter and are rarely in close proximity to Pt catalysts. This remarkably resolved structural landscape reveals that O₂ diffusion pathways in HSCs are narrower and longer than previously assumed, indicating the critical value of the carbon support redesign for optimizing cell performance.

1. Introduction

In the catalyst layers (CLs) of proton exchange membrane fuel cells (PEMFCs), the characteristics of the carbon supports have a critical influence on the durability and performance of the cost-bearing Pt(-alloy) nanocatalysts (NCs).^[1,2] Specifically, their morphological and structural properties affect the catalyst location upon deposition and their motion during operation, which are key factors of oxygen reduction reaction (ORR) kinetics, mass transport resistances, and Pt surface area degradation.^[3-6] Amongst the commonly used carbons, high surface area carbons (HSC) like Ketjenblacks (KB have become an industry standard owing to their extended interior porosity.^[5,7] These pores offer a

R. Girod, V. Tileli
Institute of Materials
École Polytechnique Fédérale de Lausanne
Lausanne CH-1015, Switzerland
E-mail: robin.girod@uantwerpen.be; vasiliki.tileli@epfl.ch
R. Girod
Present address: EMAT and NANOLight Center of Excellence
University of Antwerp
B-2020 Antwerp, Belgium

The ORCID identification number(s) for the author(s) of this article can be found under https://doi.org/10.1002/aenm.202500400

© 2025 The Author(s). Advanced Energy Materials published by Wiley-VCH GmbH. This is an open access article under the terms of the Creative Commons Attribution License, which permits use, distribution and reproduction in any medium, provided the original work is properly cited.

DOI: 10.1002/aenm.202500400

space in which most NCs are hosted while remaining inaccessible to ionomer strands, which are included to conduct protons across the CLs.[6-10] This in turns reduces the kinetic loss associated with ionomer-poisoning that more compact carbons like Vulcans typically suffer from.[11,12] Pores also anchor the catalysts and thus improve retention of electrochemically active surface area (ECSA) over time by limiting mobility and coalescence.[13] As a tradeoff, HSCs suffer from large proton and oxygen transport resistances, especially at high current densities and low cathode loadings likely associated with limited reactant diffusion or product evacuation through micropores.[11,14] Recent modeling has for instance shown that carbon pores exhibit

reduced oxygen diffusion and more chances of water occlusion as their width is decreased to the nanometer range. $^{[8,15-17]}$

Attempts to rationalize and model mass transport losses in HSCs have typically been relying on pictures of the diffusion pathways built from a combination of ensemble probes and microscopy methods. N2 physisorption isotherms fitted with density functional theory kernels have shown a distribution of pores ranging from a large population of sub-nm micropores to larger, > 10 nm, mesopores. [18–20] Electron tomography (ET), where projection images in (scanning) transmission electron microscopy (STEM) are used to compute a reconstruction of the original 3D object, is also becoming an increasingly standard technique that offers insights into Pt/C NCs and the morphology and localization of the pores. [5,7,10,21-23] In HSCs, large variations in interior porosity have been reported, with some primary particles shown to contain ≈1 nm channels connecting to the exterior while other had larger interior pores, up to 10-20 nm in diameter, opening via 2–5 nm gaps.^[7] These large openings were subsequently found to be too rare to account for sufficient oxygen diffusion.[21] Instead, slit-shaped micropores, 1-2 nm wide and 5-10 nm long, arranged concentrically in onion-like structures were observed.[21,24] It is however unclear if these pores were connected to surface openings or if diffusing gases must use the unresolved, sub-nm, pores found by N₂ physisorption. Thus, 3D images at higher resolution are needed for accurate modeling and interpretation of ensemble-averaged measurements of HSCs.

Here, we first describe the preparation method for imaging the multiscale morphology of HSCs in 3D with full-range ET, which allows minimization of reconstruction artifacts. [25–27] and

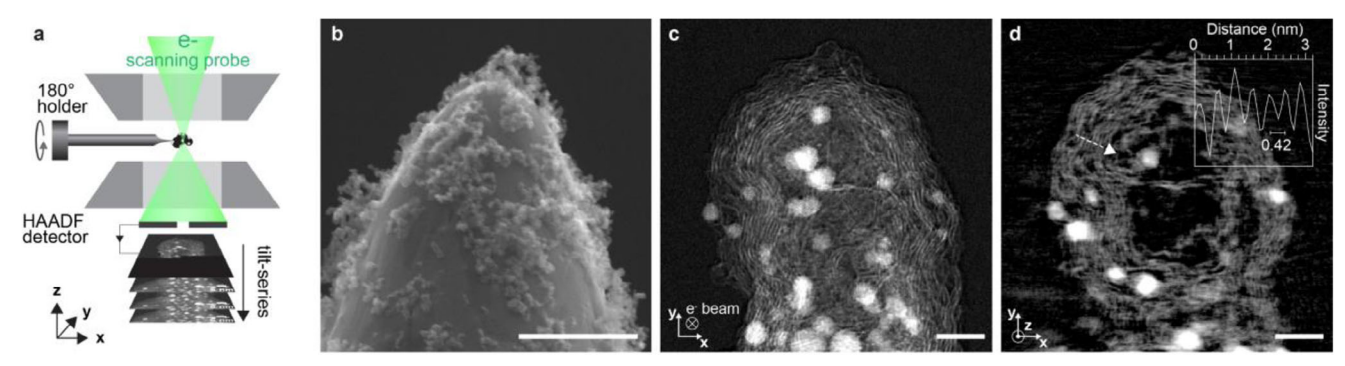


Figure 1. High resolution ET in STEM mode. a) Schematic of full-range ET acquisition in STEM mode. b) SEM image of a Pt/HSC aggregates deposited on an electropolished tungsten probe. c) Phase contrast ADF-STEM image and d) corresponding tomogram through the full-range ET reconstruction of a typical Pt/HSC aggregate. The inset is a line profile along the arrow in (d). In (c,d) the background is dark, Pt NCs are brightest and carbon has an intermediate gray intensity. Scale bars are 1 um in (b), and 5 nm in (c,d).

the alignment and reconstruction procedures that collectively enable resolving features down to individual carbon layers. The 3D reconstructions reveal a high heterogeneity of the interior carbon support structure, classified as hollow, porous, and full particles. The geometry of pores as a function of their location within the particles is reported, and we measure surface pore openings to be typically less than a nanometer in size, thus achieving a better understanding of the gas diffusion pathways in these supports.

2. Results and Discussion

2.1. High Resolution ET

In ET, a typical challenge is the limited space and tilting range available in the TEM column.^[28] This missing wedge of information elongates the reconstructed features in the direction parallel to the electron beam and, thus, reduces the resolution in this direction. Here, we used a probe holder and deposited commercial Ketjenblack HSC supports containing 19.8 wt.% Pt NCs (nominal diameter 2-3 nm) on sharp, nm-sized tungsten needles prepared by electropolishing (Figure 1a,b, methods, and Figure S1, Supporting Information). This way, the specimen was rotated on-axis through the full 180° range, removing the missing wedge (Figure S1d, Supporting Information) and providing isotropic resolution in the x-z plane (see Figure 1 for the geometry of the experiments). To visualize both carbon planes and Pt NCs, we imaged the samples in low-angle annular darkfield (LAADF) scanning (S)TEM (Figure 1c) or in high-resolution (HR)-TEM (see methods and Figure S2, Supporting Information on the merit of each mode). The tilt-series were aligned using the vertical mass fluctuation and projection-matching methods and the reconstructions were computed with iterative or regularized algorithms to optimize the signal-to-noise ratio and the contrast (methods and Figures S3 and S4, Supporting Information).

Figure 2d shows a cross-section of a 3D reconstruction from LAADF-STEM projections, where the pores, Pt NCs, and carbon structures down individual layers (inset) are clearly observed. In comparison, reconstructions from HRTEM images also resolved isolated carbon sheets, but not those in denser areas (Figure S2a, Supporting Information). We note that the imaging resolution

was close or better than the graphite d-spacing in this study (TEM at ≈ 0.3 –0.4 nm point resolution from the contrast transfer function at imaging defocus, STEM probe corrected to < 0.14 nm resolution evaluated from the FFT of an Au cross-grating grid). However, a range of other considerations may impact the reconstruction quality in a local or global, sometimes anisotropic manner. These include for example alignment quality, scan distortions, angular sampling, and adequate fulfillment of the projection requirement for tomographic reconstruction, which are further discussed in Figure S2 (Supporting Information) and Supporting information Discussion. [29]

2.2. Inter-Particles Heterogeneity

With our high resolution ET approach, we reconstructed a total of five Pt/HSC aggregates or primary particles, all shown in Figure 2a,b and further in Figure S5 (Supporting Information) and Videos S1-S5 (Supporting Information). Morphologically, the particles show strong inter-particle heterogeneity where three distinct classes can be identified. The hollow (particle 1) and porous (particle 2-4) classes have been previously reported from TEM images and ET at lower resolution. [7,21] In addition, we find other full (particle 5) particles. This classification is guided primarily by the widest pore contained in the particles (Figure 2c) and by the preferential location of Pt NCs (Figure 2b,d; Methods). In hollow particles, large mesopores are seen in the tomograms, up to 12 nm in width for particle 1. Particles from the porous class have smaller pores reaching up to 3.7, 3.8, and 5.6 nm in width for particles 2-4 respectively. Both porous and hollow classes host the majority (78-90%) of their Pt NCs in their interior. Their Pt content as measured from the segmented reconstructions can strongly vary with two porous particles ≈7– 8 wt.% and one at 24.1 wt.%. Full particles feature pores up to ≈3 nm, with all particles hosted on their exterior and a low Pt content.

Hollow and porous particles exhibit properties broadly consistent with ensemble measurements of Pt content and Pt accessibility – a proxy of interior/exterior fraction measured, for instance, electrochemically,^[10] but full particles do not.^[18] To understand their prevalence, we screened TEM images, some of which are shown in Figure S6 (Supporting Information), and counted

-and-conditions) on Wiley Online Library for rules of use; OA articles are governed by the applicable Creative Commons License

SCIENCE NEWS

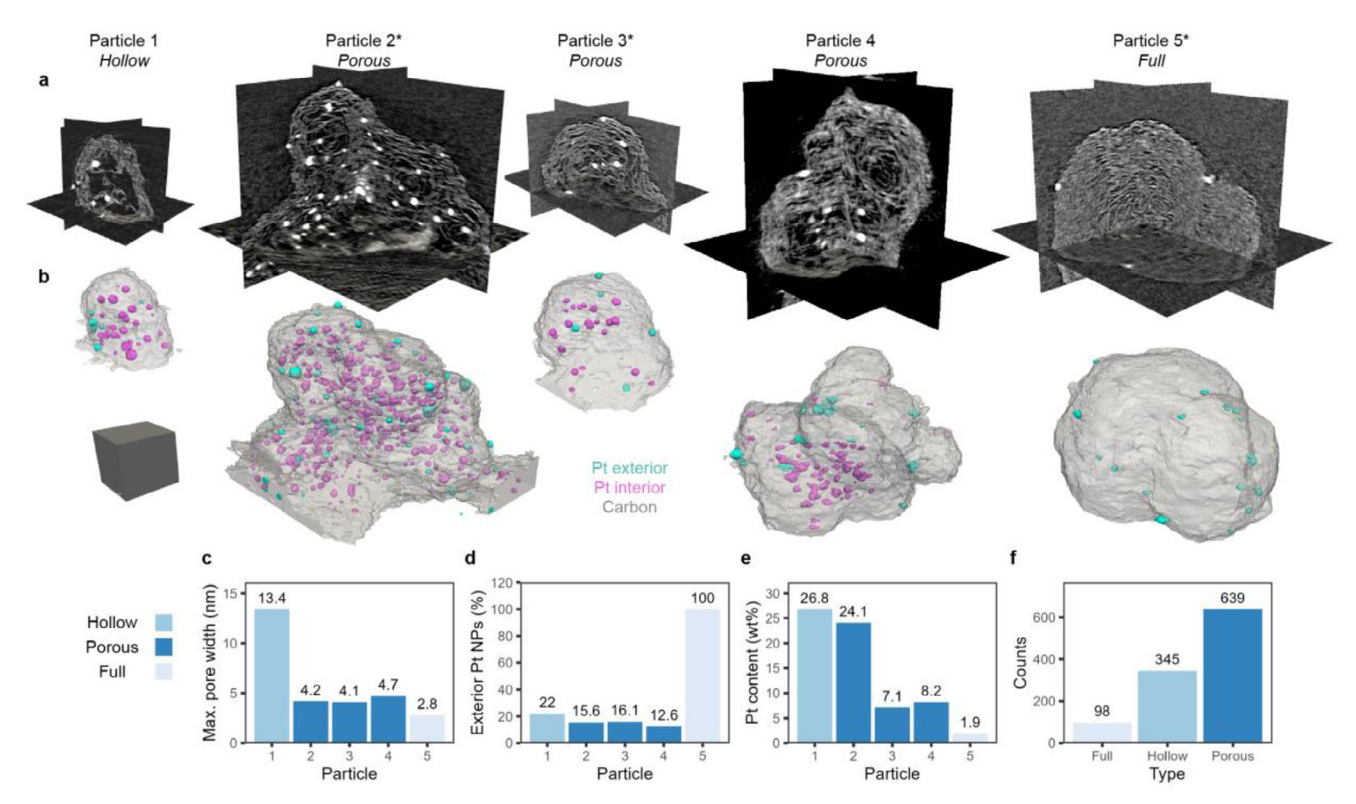


Figure 2. Overview of Pt/HSC morphologies. a) Multiorthoslice views of five HR ET reconstruction of Pt/C aggregates and b) corresponding segmented volumes with carbon (gray), interior Pt (magenta), and exterior Pt (cyan) labeled. c–e) properties of the reconstructed aggregates and f) primary particle count per type of morphology (total N = 1082) from HRTEM images. Reconstructions labeled (*) were acquired in HR-TEM mode, otherwise in ADF HR-STEM mode. The contrast of HR-TEM reconstructions was inverted to facilitate comparison. Scale cube is 20³ nm³.

the respective population of each particle profile (Figure 2f). In these measurements, only 9% of particles were full. This confirms that hollow and porous particles prevail and define the ensemble properties. We therefore focus on the reconstructions from these classes in the following.

2.3. Morphology of Interior Pores and Structures

In addition to inter-particle heterogeneity, our reconstructions also reveal a strong intra-particle one. As seen in **Figure 3a** (particle 2) and in Figure S5 (Supporting Information), the particles

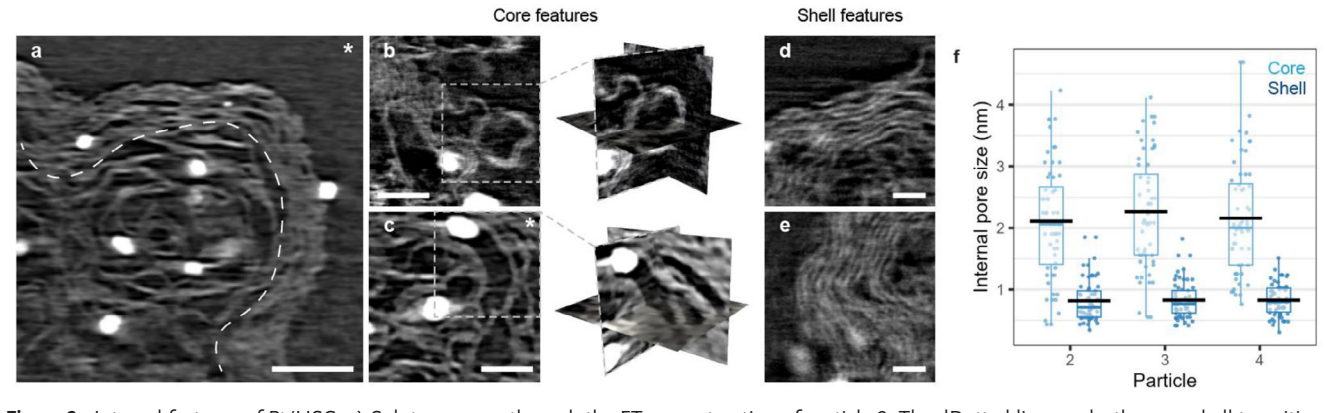


Figure 3. Internal features of Pt/HSC. a) Sub-tomogram through the ET reconstruction of particle 2. The dDotted line marks the core-shell transition. b) Close-up tomograms and multi-orthoslice view from particle 1 and c) particle 3 showing core features including spherical nodules, slit shaped pores and single layer carbon walls. d,e) Close-up tomograms from particle 1 showing the carbon plane arrangement and sub-nm pores in the shells. Images marked (*) were acquired in HR-TEM, otherwise in ADF HR-STEM. Scale bars are 10 nm in (a), 5 nm in (b,c), and 2 nm in (d,e). f) Manual measurements of pore sizes in the core and the shell of particles 2, 3, and 4. All measurements feature N = 60 points. Box plots show the quartiles, whiskers are at most 1.5 x the interquartile range, black lines show the mean. The descriptive statistics are summarized in Table S2 (Supporting Information).

16146480, Q. Downloaded from https://advanced.onlinelibary.wiley.com/doi/10.1002/aemm.202500400 by Universiteit Antwerpen, Wiley Online Library on [03/07/2025]. See the Terms and Conditions (https://onlinelibrary.wiley.com/terms-and-conditions) on Wiley Online Library for rules of use; OA articles are governed by the applicable Creative Commons Licenses

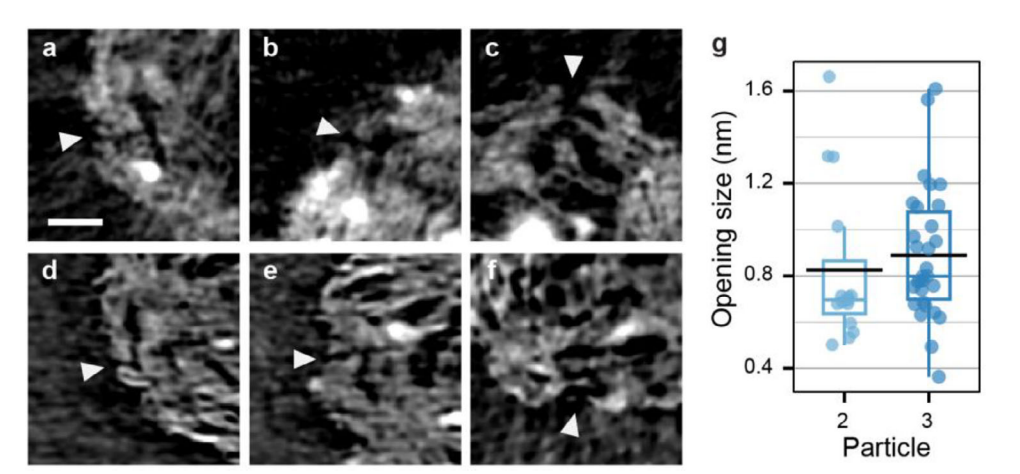


Figure 4. Openings in Pt/HSC particles. Close-up tomograms from particles 2 (a–c) and 3 (d–f) showing typical openings in HSC shells. Scale bar is 5 nm for all images. All tomograms were extracted from the HR-TEM reconstructions with contrast inverted. g) Distribution of pore opening sizes as measured manually in particles 2 (N = 16) and 3 (N = 30). Box plots show the quartiles. Whiskers are at most 1.5 x the interquartile range, black lines show the mean. The descriptive statistics are summarized in Table S3 (Supporting Information).

are well described in terms of a core-shell structure, as is commonly the case for carbon black supports. The cores enclose the largest pores, which we confirm to be separated by few-layers carbon walls, occasionally down to a single layer (Figure 3a-c). These pores are mostly isotropic in the center of the particles and are occasionally populated by fullerene-like, quasi-spherical nodules (Figure 3b). Outside of the very center and especially in the porous class, the pores become more concentric, curved and slitshaped (Figure 3a,c). Visualized in 3D, they have an oblate geometry and seem to arise from crumpled few-layers carbon sheets deposited on the initial center. Core pores typically range from 0.5 to 4 nm in width without a clear mode, as measured manually (Figure 3f). Comparison between the particles suggest that the cores of the porous class share similarities in terms of pore sizes (Figure 3f), although more complete investigations of the porosity will require its full segmentation. Qualitatively, we note that the core pores can easily be tracked through the particles, showing high connectivity.

The shells are comparatively compact, with more aligned, turbostratic carbon planes as seen in the reconstructions of particles 1 and 4 (Figure 3d,e). Their pores are also typically slit-shaped and arise from the mismatch of carbon stacks or carbon layers peeling-off (Figure 3e). The size of these shell pores typically ranges from 0.5 to 1.5 nm, with a mode $\approx\!0.6\!-\!0.8$ nm (Figure 3f). As seen in Figure S5 (Supporting Information), the diameter and thickness of the cores and the shells are also highly variable from one particle to the other, but remain relatively constant within a given aggregate.

These dimensions are consistent with pore size distribution (PSD) measurements performed with $\rm N_2$ physisorption of similar catalysts. [18–20] Specifically, the spatially unresolved sub-nm pores identified in these ensemble measurements are mostly localized within the shells in our results. In addition, compared to previously reported ET reconstructions, [21] the porous morphology of the HSCs resolved herein reveals two types of interior slitshaped pores, each with distinct PSD and structural origin. Importantly, many shell pores are significantly smaller than the 1–2 nm width typically assumed in these supports.

2.4. Openings and Reactant Diffusion Pathways

Considering the dimensions of the micropores in the shells, we then investigated if these were connecting to the exterior and could thus be used for reactant diffusion. No clear openings were found in the ADF-STEM reconstructions, possibly due to the higher dose and related beam-induced movement (Figure S2, Supporting Information). In comparison, we found tenths of pore openings in the HR-TEM reconstructions in each of the particles 2 and 3, respectively. These observations were crossvalidated in reconstructions with different algorithms (Figure S7, Supporting Information), and a representative subset is shown in Figure 4a-f. The openings were typically very narrow, with a 0.7-0.8 nm median width (Figure 4g) consistent with the size of other pores observed in the shells. Only a few openings were found to be larger than 1 nm, and none larger than 1.6-1.7 nm. Across the entire size range, only two openings, shown in Figure 4a,b, were seen to directly lead to a Pt NC, and only one, in Figure 4c, reached directly into the large and well-connected core porosity. For all other openings, including the above-nm ones, tracking the pathways between the entry points and Pt NCs was challenging, with many constrictions at the limit of resolution.

These narrow, constricted entry pathways are smaller and more tortuous than typically considered in CL modeling and likely constitute a performance bottleneck. [9,15,16] While O₂ diffusion coefficients in carbon nanotubes (CNTs) have been shown to increase for diameters below 2 nm owing to wall smoothness, [8] the real structure of HSC's sub-nm pores we show here appears rougher and more akin to mismatches between edge planes of graphitic units.[30] Smaller pores are also more prone to occlusion by water and recent modeling has shown that oxygen diffusion in partially flooded pores decreases by at least a factor 2 going from 2 to 1 nm.^[8] Thus, increasing the opening size toward the 1-2 nanometer range would increase oxygen diffusion rates while remaining small enough to prevent ionomer intrusion and outward migration of interior Pt.[9] A thinner compact shell would also provide co-benefits with a shorter, less tortuous path and less chances of occlusion by water than in long and narrow pores.[8,21]



www.advancedsciencenews.com



www.advenergymat.de

It is also possible that the very rare openings reaching directly into the core porosity, which have been more conventionally visualized and assumed, $^{[11,16]}$ contribute disproportionately to diffusion. In such pathways, transport resistance would be tied to a greater extent to the network characteristics of the central pores (connectivity, tortuosity, etc.) rather than to those of the shells. Furthermore, as these central pores are defined by few-layers sheets, they would be easily reconfigured when in contact with corrosion-catalyzing Pt. This would participate in the reduction of $\rm O_2$ transport resistance during the initial cycles of accelerated stress tests, $^{[18]}$ or after controlled oxidation. $^{[14,18,19,21,31,32]}$

Simulations would be important to establish if the number of sub-nm openings can compensate for their narrow size and allow them to sustain important diffusion fluxes, or if the more direct openings would indeed contribute disproportionately. In light of the actual structure of the supports, this task will require updated carbon models going beyond the conventional strategies of cylindrical boreholes, [15,16] nanotube-like openings, [9,33] or randomly scattered spherical pores. [30]

3. Conclusion

We have demonstrated that optimization of full-range ET can yield reconstructions of the 3D nanostructure of carbon supports at sub-nm resolution. With this approach, the core-shell nanomorphology of HSC supports can be imaged, as well as the reactant diffusion pathways within them. It was shown that openings in the compact shell range from sub-nm to rarer 1–2 nm pores and that the Pt particles typically reside far away from the openings. Most diffusion pathways in HSC supports are therefore longer, narrower and more constricted than typically assumed. Pores across the entire size range may participate or one pore type may prevail in supporting high diffusional fluxes but, either way, the characteristics of the shells (thickness, size of constrictions, etc.) and of the central pore network (connectivity, tortuosity, etc.) appear as important parameters of optimized carbons for high-power PEMFCs.

4. Experimental Section

Materials: The catalysts studied in this work were as-received, commercially available, 18.8 wt.% Pt/Ketjenblack (TEC10E20E, Tanaka Kikinzoku K.K., Japan), that had been platinized by the manufacturer. Ketjenblacks are highly porous carbon supports, and the specific surface area of this Pt/C material was previously measured to be \approx 500–550 m² g⁻¹ (ref. [18]).

Sample Preparation for Electron Microscopy: For conventional TEM imaging and ET acquisition, inks were prepared by dispersing the catalyst powders in isopropyl alcohol (analytical grade, Sigma Aldrich) or chloroform (ACS reagent, Sigma Aldrich), at 0.1 mg mL $^{-1}$ concentration. The inks were systematically sonicated in an ultrasonic bath and 2–3 μL were placed and left to dry on ultrathin lacey carbon copper grids (200 mesh, electron microscopy science) or 5 nm silicon nitride window grids with 50 \times 1500 μm^2 slots (model 76042–45, electron microscopy science).

For full-range ET, tungsten probes were fabricated in-house by electropolishing, which was a fast and inexpensive way to obtain sharp tips down to the nm range. [27,34] This choice is further motivated in the Supplementary Discussion of Figure S1 (Supporting Information). The sample preparation procedure is schematically depicted in Figure S1a (Supporting Information). Typically, a \approx 2–3 cm-long section was cut from a 1 mm

diameter tungsten wire (99.99%, Ref. 267562-15G, Sigma Aldrich). One end of this section was polished until flat and shiny on progressively finer sandpaper and SiC grinding paper. ≈5–7 mm of this tungsten probe was then immersed in a 5 mL beaker filled with 3 m KOH. The other end of the tungsten probe was connected to a potentiostat (SP-300, BioLogic) as the working electrode (WE) of the electrochemical system used for electropolishing. The counter electrode (CE) of this system was a Pd wire shaped as a coil, ≈2 cm in diameter, that was placed in the beaker to surround the immersed end of the tungsten probe. A 4 V bias was applied to the tungsten WE with respect to the CE to induce electrochemical dissolution. At this potential, the reaction at the WE was limited by mass-transport, and the solution was agitated by a magnetic stirrer at 100 rpm to accelerate this etching process. The stirring speed was chosen to maintain a still meniscus around the immersed tip while still enabling solution renewal. The size of the CE coil was chosen to ensure that H₂ evolved at the CE during the etching process does not disturb the meniscus around the probe, and the immersion depth and number of coil was chosen to ensure that the CE surface area was not limiting the currents in the system. For reference, with the geometry used here, currents at the beginning of the process were \approx 50–100 mA without stirring, and \approx 500–600 mA with. The etching process was tracked with a camera placed at the height of the meniscus but could also be followed from the decreasing currents as the tungsten surface area was progressively reduced. T, currents were down to $\approx 100-200$ mA (with agitation) when the reaction was stopped, yielding a um-sized probe within 10-15 min.

Before sample deposition, the probes were primed with a thin layer of Nafion by dipping in a Nafion D520 solution (Sigma-Aldrich), which was critical to enhance surface adhesion with Pt/C aggregates. For deposition, each probe was immersed in a freshly sonicated catalyst ink (1 mg mL $^{-1}$ in IPA or chloroform) and the results were inspected with scanning electron microscopy (SEM, Quattro, ThermoFisher Scientific). It was found that a probe radius at the apex $\approx\!0.5{-}1\,\mu\text{m}$ was best and maximized the chances of having an aggregate clearly extending out.

Electron Microscopy Imaging: HRTEM imaging was performed at a ThermoFisher Scientific F20 equipped with a Falcon III camera (ThermoFisher Scientific) and operated at 200 kV. Images for morphology screening and tilt-series acquisitions were acquired at 150 kx magnification (4096 2 pixels, 0.68 Å pixel size), with a 40 μm objective aperture and at -50-100 nm defocus.

For tomography in STEM mode, a Titan Themis (ThermoFisher Scientific) was operated at 200 kV with a 20–100 pA probe current, a 50 μm condenser aperture and an 8–15 mrad convergence angle. The ADF detector was used, with a camera length (collection angle) between 285 mm (\approx 20–125 mrad) and 910 mm (\approx 6–39 mrad) to operate in LAADF mode and adjust the balance of mass-thickness contrast and phase contrast. The acquisition mode used for each reconstruction presented in the main is summarized in Table S1 (Supporting Information).

Tomography Acquisition and Reconstruction: All tilt-series were acquired in 2° increments. For full-range ET, the specimen holder was a Fischione 2050 probe holder fitted with the on-axis cartridge for 1 mm probes. Before acquisition and to limit carbon contamination, a ≈ 15 min beam-shower was performed for all samples at a 10–20 e $^-$ nm $^{-2}$ s $^{-1}$ dose rate. The tilt-series were acquired with ThermoFisher (S)TEM tomography software.

The full-range ET acquisitions were done in two steps, with a $[-50^\circ, +50^\circ]$ tilt range each time and a $\approx 90^\circ$ manual tilt of the internal rotation mechanism of the holder in between. The exact internal rotation angle was determined in a custom-made automated procedure before assembling into one. The procedure is described in Figure S3 (Supporting Information) and associated discussion. Alignment of the series was performed with the fully automated method and software developed by Odstrčil et al. in ref. [35]. The rotation axis was determined manually by tracking a particle visible at multiple angles and was corrected to be vertical.

All tilt-series were binned by 2, with final pixel sizes summarized in Table S1 (Supporting Information). Reconstructions were computed with the filtered back projection (FBP), simultaneous iterative reconstruction technique (SIRT) or total-variation minimization (TVM). A comparison is presented in Figure S4 (Supporting Information). The method used for

www.advancedsciencenews.com



www.advenergymat.de

each reconstruction presented here is summarized in Table S1 (Supporting Information). Reconstructions with the FBP and SIRT algorithms were performed with their cuda versions of the Astra toolbox, $^{[36,37]}$ with code implemented in Python. For the SIRT reconstruction, 30–60 iterations were run. TVM reconstructions were performed using the operator discretization Python library (ODL). The L2 norm was used on the data fidelity term and the L1 norm on the TV operator, with a regularization weight $\lambda_{\rm TV}$ typically 0.02–0.1. The Douglas-Rachford solver was used with default step size and was typically run for 8–12 iterations. The forward and back projections were handled with the ASTRA cuda backend. Before the reconstruction, the tilt-series intensities were normalized to a mean and standard deviation of 1 to be able to use approximately the same hyperparameters for different reconstructions.

3D Segmentation and Analyses: Segmentation of carbon, Pt particles, background and of the largest pores was performed in 3D with a pixel classifier implemented in the Ilastik software.^[38] All intensity, edge and texture features were selected with sigma 1, 3, and 10. Surface renderings were done with Tomviz.^[39]

Pore size measurements were done manually using orthoslice views of the reconstructions. The exterior Pt fraction was evaluated by identifying particles connected to background voxels. The weight content of Pt was calculated from the number of voxels classified as carbons and Pt, using Pt and graphite densities. The pore segmentation was only used to ensure pore voxels were not counted as carbon in Pt weight fraction measurements; it was not used for pore size or morphological analyses. As detailed in the main text and in Figure S2 (Supporting Information), this is because reconstruction artefacts likely prevent the full identification of the smallest pores. These small pores were of limited influence for volumetric measurements like weight fraction, but would strongly impact surface and automated pore size distribution measurements.

Supporting Information

Supporting Information is available from the Wiley Online Library or from the author.

Acknowledgements

The authors thank Timon Lazaridis, Prof. Hubert Gasteiger and Dr. Victor Boureau for assistance and discussions. Funding: The work was supported by the Swiss National Science Foundation (SNF) under award no. CRSII5 180335.

Conflict of Interest

The authors declare no conflict of interest.

Data Availability Statement

The dataset and the code used or created for this study are available at https://doi.org/10.5281/zenodo.15564040.

Keywords

carbon catalyst supports, diffusion pathways, full-range electron tomography, proton exchange membrane fuel cells

Received: January 20, 2025 Revised: April 15, 2025 Published online:

- [1] K. Jiao, J. Xuan, Q. Du, Z. Bao, B. Xie, B. Wang, Y. Zhao, L. Fan, H. Wang, Z. Hou, S. Huo, N. P. Brandon, Y. Yin, M. D. Guiver, *Nature* 2021, 595, 361.
- [2] D. A. Cullen, K. C. Neyerlin, R. K. Ahluwalia, R. Mukundan, K. L. More, R. L. Borup, A. Z. Weber, D. J. Myers, A. Kusoglu, *Nat. Energy* 2021, 6, 462
- [3] S. Holdcroft, Chem. Mater. 2014, 26, 381.
- [4] S. Sui, X. Wang, X. Zhou, Y. Su, S. Riffat, C. Liu, J. Mater. Chem. A 2017. 5, 1808.
- [5] B. T. Sneed, D. A. Cullen, K. S. Reeves, O. E. Dyck, D. A. Langlois, R. Mukundan, R. L. Borup, K. L. More, ACS Appl. Mater. Interfaces 2017, 9, 29839.
- [6] Y.-C. Park, H. Tokiwa, K. Kakinuma, M. Watanabe, M. Uchida, J. Power Sources 2016, 315, 179.
- [7] E. Padgett, N. Andrejevic, Z. Liu, A. Kongkanand, W. Gu, K. Moriyama, Y. Jiang, S. Kumaraguru, T. E. Moylan, R. Kukreja, D. A. Muller, J. Electrochem. Soc. 2018, 165, F173.
- [8] N. Kikkawa, M. Kimura, Langmuir 2024, 40, 1674.
- [9] N. Kikkawa, R. Jinnouchi, J. Phys. Chem. C 2022, 126, 11518.
- [10] R. Girod, T. Lazaridis, H. A. Gasteiger, V. Tileli, Nat. Catal. 2023, 6, 383
- [11] N. Ramaswamy, W. Gu, J. M. Ziegelbauer, S. Kumaraguru, J. Electrochem. Soc. 2020, 167, 064515.
- [12] K. Shinozaki, Y. Morimoto, B. S. Pivovar, S. S. Kocha, J. Power Sources 2016, 325, 745.
- [13] E. Padgett, V. Yarlagadda, M. E. Holtz, M. Ko, B. D. A. Levin, R. S. Kukreja, J. M. Ziegelbauer, R. N. Andrews, J. Ilavsky, A. Kongkanand, D. A. Muller, J. Electrochem. Soc. 2019, 166, F198.
- [14] V. Yarlagadda, M. K. Carpenter, T. E. Moylan, R. S. Kukreja, R. Koestner, W. Gu, L. Thompson, A. Kongkanand, ACS Energy Lett. 2018. 3, 618.
- [15] R. Zuo, L. Fan, J. Wang, Q. Du, K. Jiao, Energy 2024, 307, 132624.
- [16] J. You, Z. Zheng, X. Cheng, H. Li, C. Fu, L. Luo, G. Wei, S. Shen, X. Yan, J. Zhang, ACS Appl. Mater. Interfaces 2023, 15, 21457.
- [17] C. J. C. Otic, S. Katayama, M. Arao, M. Matsumoto, H. Imai, I. Kinefuchi, ACS Appl. Mater. Interfaces 2024, 16, 20375.
- [18] T. Lazaridis, H. A. Gasteiger, J. Electrochem. Soc. 2021, 168, 114517.
- [19] T. Lazaridis, H. A. Gasteiger, J. Electrochem. Soc. 2024, 171, 094506.
- [20] N. Ramaswamy, B. Zulevi, G. McCool, Z. Shi, A. Chavez, D. A. Muller, A. Kongkanand, S. Kumaraguru, ACS Appl. Eng. Mater. 2023, 1, 2543.
- [21] M. Ko, E. Padgett, V. Yarlagadda, A. Kongkanand, D. A. Muller, J. Electrochem. Soc. 2021, 168, 024512.
- [22] Y. Peng, J.-Y. Choi, T. Fürstenhaupt, K. Bai, Y. Zhang, D. Banham, J. Mater. Chem. A 2021, 9, 13471.
- [23] T. Ito, U. Matsuwaki, Y. Otsuka, M. Hatta, K. Hayakawa, K. Matsutani, T. Tada, H. Jinnai, Electrochemistry 2011, 79, 374.
- [24] L. Amichi, H. Yu, A. Ziabari, O. Rahman, D. Arregui-Mena, L. Hu, K. C. Neyerlin, D. A. Cullen, Adv. Energy Mater. 2024, 14, 2402310.
- [25] E. Padgett, R. Hovden, J. C. DaSilva, B. D. A. Levin, J. L. Grazul, T. Hanrath, D. A. Muller, Microsc. Microanal. 2017, 23, 1150.
- [26] T. Przybilla, B. A. Zubiri, A. M. Beltrán, et al., Small Methods 2018, 2,
- 1700276. [27] X. Huang, Y. Tang, C. Kübel, D. Wang, *Microsc. Microanal.* **2022**, *28*,
- 1981.
 [28] R. K. Leary, P. A. Midgley, in, Springer Handbook of Microscopy (Eds.: P. W. Hawkes, J. C. H. Spence), Springer International Publishing,
- [29] J. Frank, Electron Tomography: Methods for Three-Dimensional Visualization of Structures in the Cell, Springer, New York, London
- [30] S. Ban, K. Malek, C. Huang, Z. Liu, Carbon 2011, 49, 3362.

Cham 2019.

- [31] S. Ott, A. Orfanidi, H. Schmies, B. Anke, H. N. Nong, J. Hübner, U. Gernert, M. Gliech, M. Lerch, P. Strasser, Nat. Mater. 2019, 19, 77.
- [32] S. Zhang, F. Zhou, B. Luo, J. Tan, M. Pan, Energy Fuels 2024, 38, 9046.

ADVANCED ENERGY MATERIALS

www.advancedsciencenews.com

www.advenergymat.de

- [33] F. C. Cetinbas, R. K. Ahluwalia, N. N. Kariuki, V. De Andrade, D. J. Myers, J. Electrochem. Soc. 2020, 167, 013508.
- [34] B.-F. Ju, Y.-L. Chen, Y. Ge, Rev. Sci. Instrum. 2011, 82, 013707.
- [35] M. Odstrčil, M. Holler, J. Raabe, Opt. Express 2019, 27, 36637.
- [36] W. van Aarle, W. J. Palenstijn, J. De Beenhouwer, T. Altantzis, S. Bals, K. J. Batenburg, J. Sijbers, *Ultramicroscopy* 2015, 157, 35.
- [37] W. J. Palenstijn, K. J. Batenburg, J. Sijbers, J. Struct. Biol. 2011, 176, 250.
- [38] S. Berg, D. Kutra, T. Kroeger, C. N. Straehle, B. X. Kausler, C. Haubold, M. Schiegg, J. Ales, T. Beier, M. Rudy, K. Eren, J. I. Cervantes, B. Xu, F. Beuttenmueller, A. Wolny, C. Zhang, U. Koethe, F. A. Hamprecht, A. Kreshuk, *Nat. Methods* 2019, 16, 1226.
- [39] B. D. A. Levin, Y. Jiang, E. Padgett, S. Waldon, C. Quammen, C. Harris, U. Ayachit, M. Hanwell, P. Ercius, D. A. Muller, R. Hovden, *Microscopy Today* 2018, 26, 12.